

NUMERICAL STUDY OF BUBBLE COALESCENCE IN SUB-COOLED FLOW BOILING

Eyitayo James Owoeye and DuWayne Schubring

Department of Mechanical and Aerospace Engineering, University of Florida
205 Nuclear Science Building, P.O. Box 116300, Gainesville FL 32611-6300, USA
msgenius10@ufl.edu and dlschubring@ufl.edu

ABSTRACT

Bubble collisions, coalescence, and break-up are significant phenomenon observed in the cooling channels of a nuclear reactor. Coalescence can occur along the rod surface as the bubbles nucleate, grow, and slide upward. After the detached bubbles are far away from the wall, including during bubble condensation in sub-cooled boiling, further collisions and coalescence can occur. Understanding the interaction of isolated bubbles can lead to increased cooling efficiency and prevention of critical heat flux conditions. In this study, simulation of isolated bubble coalescence and motion in an upward sub-cooled flow is performed in 3D using the open-source code OpenFOAM. Bubble-bubble interaction is investigated in laminar and turbulent flow conditions with large eddy simulation (LES) and volume-of-fluid (VOF) interface tracking method. Steam-water flow is varied at different system pressures that include the pressures observed in pressurized water reactors (PWRs) and boiling water reactor (BWRs). The study is carried out for both geometric cases noted above (near-wall and in bulk fluid). The behavior of consecutive leading and trailing bubbles before and after merging is investigated. Interaction of adjacent bubbles on the same vertical level is also modeled. Bubble dynamics, distortion, and coalescence time are also analyzed as functions of system pressure, bubble size, and bulk velocity.

KEYWORDS

Coalescence, Lift-off, LES, Sub-cooled boiling, VOF, Bubble dynamics

1. INTRODUCTION

Most industrial applications of boiling heat transfer involve multiple bubbles existing in the same system simultaneously. Controlling the heat transfer during bubble collision and coalescence can lead to improved cooling efficiency in a nuclear reactor. To understand the interactions between bubbles in subcooled flow boiling, the study will consider two consecutive and adjacent bubbles. The process of bubble coalescence occurs in three stages; First, the bubbles collide by trapping a small amount of liquid between them. Next, this liquid film drains into the bubbles until the film reaches a critical thickness. Finally, the liquid film ruptures causing the bubbles to coalesce [1, 2].

Bubble coalescence is classified in three categories. Coalescence can occur far away from the heated wall between adjacent rising bubbles at the same height or between consecutive rising bubbles with bubble at the top having a lower velocity. Coalescence can also occur between consecutive bubbles near the wall when the rate of growth of a bubble is higher than the rise velocity of the previous bubble, thereby resulting in a single bubble that is elongated vertically. Lastly, coalescence can occur when adjacent bubbles growing on a heated wall merge due to growth [3].

Situ et al. [4] studied bubble merging in flow boiling in a vertical annular channel. They reported that bubbles coalesced close to a nucleation site due to their low axial velocity near the wall, thereby resulting in reduced bubble departure frequency. Bonjour et al. [3] also experimentally investigated the thermal effect of bubble coalescence from artificial nucleation sites in pool boiling. A decrease in bubble frequency as a result of coalescence occurred for moderate heat flux while the frequency increases with increasing heat flux, for low or high heat flux ranges.

Golobic et al. [5] examined changes in heat transfer from the wall contact area during horizontal coalescence between bubbles of dissimilar size using heated titanium foil. They observed that coalescence caused a local reduction in heat flux near the contact area. This occurred due to reflooding of the precooled contact area by lateral motion of a superheated wall layer of liquid coming from the surrounding region at high superheat. The asymmetric behavior between bubbles before coalescence indicated that heat transfer occurred from the entire contact area, not just the triple-contact zone. The triple-contact zone is the region where the solid wall, film liquid, and vapor bubble come in contact with each other. The region where the bubble touches the wall is termed the contact area.

Chen et al. [6] performed 2-D numerical simulation of the coalescence and motion of bubble pairs rising in a stationary liquid using the moving particle semi-implicit (MPS) method. They observed that the rising velocity of the trailing bubble was higher than that of the leading bubble, even though both bubbles rose faster than the isolated bubble. Wei et al. [1] studied bubble coalescence using VOF interface tracking method. The liquid-vapor interface was captured with the PLIC geometric restructuring method. It was observed that a small bubble with a higher pressure is sucked into a bubble with a lower pressure. The relative motion of the two bubbles generated two symmetric vortices and a stagnant region that disappeared after coalescence was complete.

This study focuses on the numerical modeling of the coalescence behavior of two bubbles at pressures of 1 – 21 MPa using numerical method. This is due to its application to nuclear reactor cooling. The analysis was done using interface compression model of VOF method, while turbulence was modeled using one-equation eddy viscosity LES model. The study was performed by varying system pressure, bubble size, bubble spacing and orientation, and bulk velocity. The average velocity of the bubbles before and after coalescence was obtained. Bubble coalescence time, lift-off time, and distortion were also studied. The analysis was performed using OpenFOAM [7].

2. GOVERNING EQUATIONS

2.1 Macro-region Analysis

The numerical study of bubble growth was performed using VOF – interface compression method, coupled with adaptive mesh refinement (AMR). Liquid and vapor phases were considered as individually incompressible. To study the turbulence behavior, large energy-containing structures were resolved on the computational grid while the unresolved sub-grid structures were modeled using LES. The volume fraction α , in each computational cell, was defined in the following form:

$$\alpha = \begin{cases} 1 & \text{liquid phase} \\ 0 < \alpha < 1 & \text{interface} \\ 0 & \text{vapor phase} \end{cases} \quad (1)$$

The continuity equation used for tracking the volume fraction is:

$$\frac{\partial \alpha}{\partial t} + \vec{u} \nabla \alpha + \underbrace{\nabla \cdot (\vec{u}_c \alpha (1 - \alpha))}_A = \frac{\dot{m}_{ev} - \dot{m}_c + \dot{m}_m}{\rho} \quad (2)$$

where ρ and \vec{u} are the fluid density and velocity respectively. \dot{m}_{ev} , \dot{m}_c , and \dot{m}_m denote mass source terms due to evaporation, condensation, and micro-region analysis respectively. A is an artificial compression term used to limit α between 0 and 1 and ensure numerical stability. The compressive velocity \vec{u}_c , is based on the maximum velocity at the interface. It is only active at the interface and suitable to compress the interface as defined below [8].

$$\vec{u}_c = \min [c_\alpha |\vec{u}|, \max(|\vec{u}|)] \frac{\nabla \cdot \alpha}{|\nabla \cdot \alpha|} \quad (3)$$

The intensity of compression is controlled by a compression factor c_α , which gives no compression if it is zero, a conservative compression for $c_\alpha = 1$, and enhanced compression when $c_\alpha > 1$. For this paper, $c_\alpha = 1$ is applied. The fluid density, ρ at each interface is computed from the properties of the two phase.

$$\rho = \alpha_l \rho_l + (1 - \alpha_l) \rho_g \quad (4)$$

where subscripts l and g denote liquid and vapor phases, respectively. Other fluid properties such as specific heat capacity c_p , thermal conductivity λ , and kinematic viscosity ν , are computed in similar manner at the interface. A single incompressible momentum equation is solved for all cells, producing a shared velocity field between the phases.

$$\frac{\partial(\rho \vec{u})}{\partial t} + \nabla \cdot (\rho \vec{u} \times \vec{u}) = -\nabla P + \nabla \cdot [\mu_{eff}(\nabla \vec{u} + \nabla \vec{u}^T)] + \rho \vec{g} + \sigma \kappa \nabla \alpha \quad (5)$$

P , σ , and κ denote the pressure, surface tension, and curvature of interface, respectively. The effective dynamic viscosity is defined as $\mu_{eff} = \rho \nu_{eff}$ where ν_{eff} is modeled in sub-section 2.4. The curvature of the interface is given as:

$$\kappa = -\nabla \cdot \left(\frac{\nabla \alpha}{|\nabla \alpha|} \cdot S_f \right) \quad (6)$$

S_f is the surface vector of the cell face at the interface. The static contact angle θ of the volume fraction at the wall boundary is defined as the angle between the interface normal and face unit normal \vec{n}_f at the wall. This is corrected at each time step when computing the curvature.

$$\cos \theta = \frac{\nabla \alpha}{|\nabla \alpha|} \cdot \vec{n}_f \quad (7)$$

To account for the heat transfer, the total energy equation with temperature T was computed as:

$$\begin{aligned} & \frac{\partial [\rho (c_p T + \frac{\vec{u}^2}{2})]}{\partial t} + \nabla \cdot \left[\rho \vec{u} \left(c_p T + \frac{\vec{u}^2}{2} \right) \right] = \nabla \cdot (\lambda_{eff} \nabla T) + \frac{\partial P}{\partial t} + \rho \vec{g} \cdot \vec{u} \\ & + \underbrace{\sigma \kappa \frac{\partial \alpha}{\partial t} + T \left(\frac{\partial \sigma}{\partial T} \right) \left(\frac{\partial a_i}{\partial t} + \vec{u} \cdot (\nabla \cdot a_i) \right)}_B + \underbrace{\tau : \nabla \vec{u} + \vec{u} \cdot (\nabla \cdot \tau)}_C + \underbrace{(\dot{m}_{ev} - \dot{m}_c + \dot{m}_m) h_{fg}}_D \end{aligned} \quad (8)$$

The terms B, C, and D represent the effect of surface tension, turbulence, and interfacial heat transfer, respectively, while a_i is the interfacial area concentration. The symmetric stress tensor τ , is defined as:

$$\tau = -\mu_{eff} \left[\nabla \vec{u} + \nabla \vec{u}^T - \frac{2}{3} (\nabla \cdot \vec{u}) \mathbf{I} \right] \quad (9)$$

The effective thermal conductivity λ_{eff} is defined as follows:

$$\lambda_{eff} = \lambda + \rho c_p \frac{\nu_{sgs}}{Pr_t} \quad (10)$$

where ν_{sgs} is SGS kinematic viscosity given by:

$$\nu_{sgs} = c_k \sqrt{k} \Delta \quad (11)$$

Δ is proportional to the wavelength of the smallest scale retained by the LES filtering operation. k is the turbulent kinetic energy while scalar constant, $c_k = 0.094$.

To account for two-phase flow, the turbulent Prandtl number Pr_t is defined as:

$$Pr_t = \alpha_l \underbrace{\left(0.85 + \frac{100}{Pr_l Re_b^{0.888}}\right)}_E + (1 - \alpha_l) \left(0.85 + \frac{100}{Pr_g Re_b^{0.888}}\right) \quad (12)$$

The term E, in eq. 12 represents the original Pr_t model for single phase developed by Weigand et al. [9]. Pr_l and Pr_g are the liquid and vapor Prandtl numbers, respectively. The bubble Reynolds number Re_b , is given as:

$$Re_b = \frac{\rho_l u_{rel} D_s}{\mu_l} \quad \text{where} \quad u_{rel} = \left[(u_{b,x})^2 + (u_{b,y})^2 + (u_{b,z} - u_{l,z})^2 \right]^{1/2} \quad (13)$$

u_{rel} is the bubble relative velocity while $u_{b,x}$, $u_{b,y}$, and $u_{b,z}$ are the instantaneous bubble velocities in the transverse (x), normal (y), and axial (z) directions respectively. $u_{l,z}$ is the local axial (bulk) velocity. The Sauter mean diameter D_s is defined as shown where the bubble surface area A_b , is computed by defining an iso-surface that has a mean volume fraction, i.e. $\alpha = 0.5$.

$$D_s = 6 \frac{\sum_j \alpha_j V_j}{A_b} \quad (14)$$

2.2 Micro-region analysis

The bubble microlayer is a thin liquid film between the bubble and heated wall. It accounts for a significant portion of the heat transferred to the bubble. To model this micro-region, a control volume analysis around the microlayer thickness, δ , was performed. δ is approximately four times smaller than the bubble mesh size. Interfacial shear stress at the liquid-vapor interface was assumed to be negligible. Separate mass conservation, momentum and energy equations are solved for the micro-region as given below [10].

$$\frac{\dot{q}}{\rho_l h_{fg}} = -\frac{1}{r} \frac{\partial}{\partial r} \int_0^\delta r u_r dy \quad (15)$$

$$\frac{\partial P_l}{\partial r} = \mu_l \frac{\partial^2 u_r}{\partial y^2} \quad (16)$$

$$\dot{q} = \frac{\lambda_l (T_w - T_{int})}{\delta} \quad (17)$$

The evaporative heat flux was applied using the modified Clausius Clapeyron equation, as:

$$\dot{q} = h_{ev} \left[T_{int} - T_g + \frac{(P_l - P_g)T_v}{\rho_l h_{fg}} \right] \quad \text{where} \quad h_{ev} = (2/\pi R_g T_g)^{0.5} \rho_g h_{fg}^2 / T_g \quad (18)$$

The following boundary conditions were applied:

$$u_r|_{y=0} = 0, \quad \frac{\partial u_r}{\partial y}|_{y=\delta} = 0$$

The pressures in the vapor and liquid phases satisfy the following relation:

$$P_l = P_g - \sigma \kappa - \frac{A}{\delta^3} + \frac{\dot{q}^2}{\rho_g h_{fg}^2} \quad (19)$$

where the Hamaker constant, A is 10^{-20} J [10]. Similar to eq. (6), the interface curvature is defined as:

$$\kappa = \frac{1}{r} \frac{\partial}{\partial r} \left[r \frac{\partial \delta}{\partial r} / \sqrt{1 + \left(\frac{\partial \delta}{\partial r} \right)^2} \right] \quad (20)$$

Combining eqns. (15 – 17) results in a 4th-order microlayer thickness equation [10]:

$$\delta'''' = f(\delta, \delta', \delta'', \delta''') \quad (21)$$

where \prime denotes $\partial/\partial r$. To compute the 4th-order ode, these boundary conditions were applied.

$$\text{when } r = r_0, \quad \delta = \delta_0, \quad \delta' = \delta'' = 0 \quad \text{when } r = r_1, \quad \delta'' = 0$$

Using the numerical solution of δ , the interfacial mass transferred from the microlayer is:

$$\dot{m}_m = \int_{r_0}^{r_1} \frac{\lambda(T_w - T_{int})}{h_{fg} \Delta V_m \delta} r dr \quad (22)$$

where ΔV_m is a control volume of the vapor near the micro-region. \dot{m}_m is then added to the evaporation source terms to complete the total mass transfer to the bubble.

2.3 Modeling of Source Terms

The source terms were computed by assuming that heat and mass transfer occur at the interfacial cell due to temperature gradient. This transfer depends on the saturated temperature, T_{sat} [1]. If $T \geq T_{sat}$, evaporation occurs. Mass of the liquid phase decreases while mass of the vapor phase increases correspondingly, resulting in bubble growth. The mass transferred at each interface cell is given as [10]:

$$\dot{m}_{ev} = (1 - \alpha) \frac{\lambda \nabla T}{h_{fg}} |_{T \geq T_{sat}} \cdot \frac{\nabla \rho}{\rho} \quad (23)$$

where T is the local liquid temperature at the cell while λ is computed similar to eq. (4). The heat transfer at each cell is obtained by multiplying \dot{m}_{ev} with h_{fg} .

When $T < T_{sat}$, condensation occurs. The mass of liquid phase increases while the mass of the vapor phase decreases correspondingly, therefore the bubble shrinks. The mass transferred from the vapor to the bulk liquid is:

$$\dot{m}_c = \alpha \frac{\lambda \nabla T}{h_{fg}} |_{T < T_{sat}} \cdot \frac{\nabla \rho}{\rho} \quad (24)$$

2.4 LES Turbulence Model

The One Equation Eddy Viscosity model was used to model the unresolved turbulence scale. It applies a modeled balanced equation to simulate the behavior of turbulent kinetic energy, k , in incompressible flow using the Eddy viscosity sub-grid scale (SGS) field model as given below [11].

$$\frac{\partial k}{\partial t} + \nabla \cdot (\vec{u}k) = \nabla \cdot (v_{eff} \nabla k) + G - \frac{c_e k^{3/2}}{\Delta} \quad (25)$$

where v_{eff} is the effective kinematic viscosity defined as $v_{eff} = \nu + v_{sgs}$. G is defined as follows:

$$G = 2v_{sgs} |\nabla u|^2 \quad (26)$$

v_{sgs} is the defined in eq. 11 while scalar constant, $c_e = 1.048$.

2.5 Near-Wall Treatment

A boundary layer is created on the adjacent wall when flow velocity changes from the no-slip condition at the walls to its free-stream value. The structure of turbulent boundary layer exhibits a large velocity gradient compared to flow at the core region, hence near-wall treatment is needed. The standard logarithmic law is the most common approach for near-wall treatment but it cannot account for moderate to strong non-equilibrium wall functions, lacks pressure gradient sensitivity, and requires a minimum value $y^+ \approx 30$. An alternative is the Spalding's law [12] which fits the laminar, buffer, and logarithmic regions of an equilibrium boundary layer. The turbulence length-scale, y^+ is defined as follows:

$$y^+ = u^+ + \frac{1}{E} \left[e^{cu^+} - 1 - cu^+ - \frac{(cu^+)^2}{2} - \frac{(cu^+)^3}{6} \right] \quad (27)$$

where $E = 9.8$ and $c = 0.41$. y^+ and u^+ are normalized as:

$$y^+ \equiv \frac{yu_\tau}{\nu} \quad \& \quad u^+ \equiv \frac{u}{u_\tau} \quad (28)$$

u_τ and y are the shear velocity and boundary layer length respectively. Using $u|_{y=0} = 0$, the wall shear stress τ_w is:

$$\tau_w = \rho u_\tau^2 = \rho (v_{sgs} + \nu) \frac{u}{y} \quad (29)$$

The turbulent kinematic viscosity at the wall ν_w is obtained as:

$$\nu_w = \nu \left(\frac{u}{u^+} y^+ - 1 \right) \quad (30)$$

$y^+ \approx 11$ is used at the first cell to ensure that the near-wall region is within the buffer region.

An iterative process is used to obtain the solution of u_τ from eqn. (27) since it is non-linear. This is performed using Newton-Raphson method, which converges rapidly to a tight tolerance when applied.

$$u_\tau = u_\tau^{n-1} - \frac{f}{f'} \quad (31)$$

where u_τ^{n-1} is the shear velocity from the previous iteration while f and f' are defined as follows:

$$f = u^+ - y^+ + \frac{1}{E} \left[e^{cu^+} - 1 - cu^+ - \frac{(cu^+)^2}{2} - \frac{(cu^+)^3}{6} \right] \quad (32)$$

$$f' = -\frac{u^+}{u_\tau} - \frac{y^+}{u_\tau} - \frac{1}{E} \left[\frac{cu^+}{u_\tau} e^{cu^+} - \frac{cu^+}{u_\tau} - \frac{(cu^+)^2}{u_\tau} - \frac{(cu^+)^3}{2u_\tau} \right] \quad (33)$$

3. NUMERICAL PROCEDURE

The computational domain was generated with Cartesian mesh. It consists of a vertical cylinder with diameter 5 mm which contains upward flow. Fig. 1 (*left*) shows two consecutive bubbles with contact angle θ , separated by distance, d along a vertical pipe wall. A constant value of $\theta = 18^\circ$ is applied in this study, which is the contact angle of copper surface. The right image shows the mesh around the bubbles.

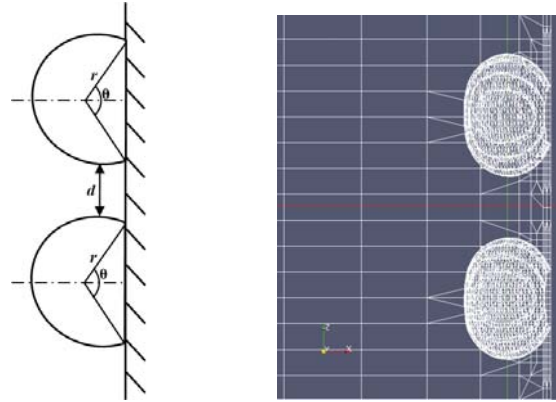


Figure 1: Images illustrating the notations (*left*) and meshes (*right*) around two consecutive bubbles

A nominal mesh size of $40 \mu\text{m}$ with 3017 meshes was applied to capture the coalescence and dynamics of each bubble. This was implemented using h – adaptivity numerical solution for adaptive mesh refinement (AMR). A fixed uniform velocity field was used at the inlet, zero gradient at outlet, and no slip was along on the wall. Constant heat flux was applied on all domain faces for the temperature field. A fixed uniform pressure was applied at the outlet and zero gradient at the inlet and walls. The turbulent kinetic energy and SGS kinematic viscosity were initialized as shown:

$$k_{ini} = \frac{3}{2}(u_{bulk}I)^2, \quad \nu_{sgs,ini} = c_k \sqrt{k}l_m \quad (34)$$

The initial turbulence intensity is $I = 0.16Re^{-1/8}$ and turbulence length scale is $l_m = 0.07D_{pipe}$. They estimate the turbulence characteristics in a fully-developed duct flow. The study was performed using the properties of steam and water at pressure range of 1 – 21 MPa [13].

The macrolayer equations were solved implicitly with finite volume method using the PIMPLE algorithm. The pressure matrix equation matrix was solved using preconditioned conjugate gradient (PCG) linear solver with a diagonal incomplete-Cholesky (DIC) smoother. The void fraction, velocity, and temperature matrix equations were solved using preconditioned bi-conjugate gradient (PBiCG) linear solver with DIC preconditioner. Adjustable time step of $2.8 - 12 \mu\text{s}$ was applied using a Courant number of 0.5. The microlayer equation was computed using MATLAB ODE solver for boundary value problem, *bvp4c*. It uses finite difference method to implement the 3-stage Lobatto IIIa formula.

4. NUMERICAL VALIDATION

The numerical method was qualitatively validated with experimental results from the open literature. Quantitative validation could not be performed due to inadequate experimental data. This validation was performed for two consecutive and two adjacent bubbles. The experiments conducted at zero bulk

velocity and adiabatic condition. The fluid properties used are $\rho_l = 817 \text{ kg/m}^3$, $\rho_g = 0.711 \text{ kg/m}^3$, $\sigma = 16.9 \text{ mN/m}$, and $\nu = 1.0 \text{ cSt}$ [6]. Fig. 2 compares the coalescence images of [14] with the numerical result. The adjacent bubbles, already detached from the wall, each had a diameter of 1.8 mm and initial spacing, $d = 0.2 \text{ mm}$.

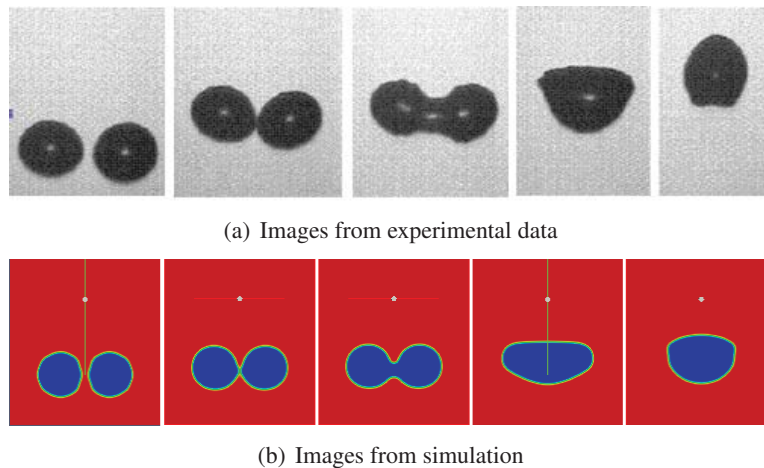


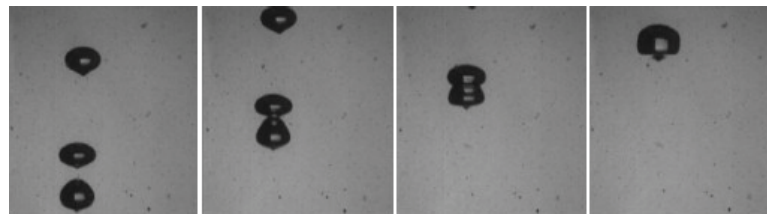
Figure 2: Images comparing the coalescence of adjacent bubbles between experimental data and numerical results at approx. $t = 0, 7.48, 8.42, 10.48, \& 13.48 \text{ ms}$

Next, the coalescence of consecutive leading and trailing bubbles is compared using images from [15]. Fig. 3 compares the images of bubbles with diameter of 6 mm and initial spacing, $d = 6 \text{ mm}$. Note that the validation is only for the two lower bubbles in the Fig. 3(a). The leading and trailing bubbles got closer to each other as the rose. This attraction was due to the presence of a larger wake of the leading bubble which decreased the drag force of the trailing bubble [6]. At $t = 91.1 \text{ ms}$, the bubbles came in close contact and then coalesced at $t = 95.2 \text{ ms}$. Due to the sudden increase in volume, the new bubble experienced a shape change as shown at $t = 108 \text{ ms}$. The bubble topologies in Figs. 2 & 3 show similar behavior of the bubbles before and after coalescence. It indicates a good qualitative agreement between the numerical method and experimental results.

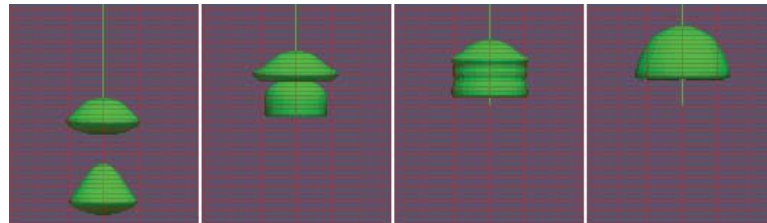
5. RESULTS AND DISCUSSION

The focus of this work is to study the coalescence behavior of bubbles at pressures between 1 – 21 MPa due to its applicability to the cooling of a light water reactor. For easy comparison, a base case was maintained using two 0.5 mm bubble diameters with the following flow conditions: $d = 0.2 \text{ mm}$, $P = 6.9 \text{ MPa}$, $\theta = 18^\circ$, $\dot{q} = 0.5 \text{ MW/m}^2$, $\Delta T_{sub} = 10 \text{ K}$, and zero bulk velocity. The coalescence behavior of the bubble pairs are investigated by varying these flow condition parameters.

The process that occurs during coalescence of bubble pair is depicted in Fig. 4. First, the bubbles are attached to each other due to the presence of large wake of the leading bubble. Next, a small amount of liquid is trapped between the bubbles when they collide as shown in the second image. This thin film of liquid is then drained out until a critical thickness is reached when the liquid film ruptures causing the bubbles to coalesce as given in the third image. Finally, as a result of the sudden increase in volume of the newly formed bubble, it undergoes a change in topology into a more stable shape and oscillates during the process.



(a) Images from experimental data (for the two lower bubbles)



(b) Images from simulation

Figure 3: Images comparing the coalescence of consecutive bubbles between experimental data and numerical results at approx. $t = 63.4, 91.1, 95.2, \& 108$ ms

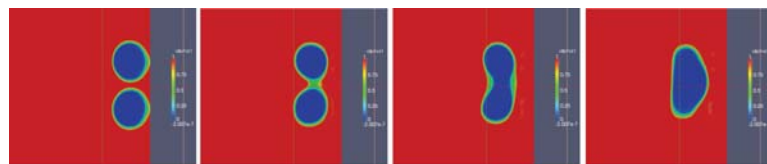


Figure 4: Stages of bubble coalescence

Coalescence may however not occur if the bubbles are far apart. Also, some bubbles may bounce off each other if the contact time is less than time needed to drain the thin liquid film [16]. This usually occurs at high surface tension but this work focuses on high pressure (low surface tension) conditions.

5.1 Effect of Bubble Spacing and Orientation

The impact of initial spacing and orientation of the bubble pairs was investigated. Fig. 5(a) shows the average velocity of the bubbles before and after collision, when the vertical distance between the bubble pair is varied. The average velocity was obtained by computing the average of the instantaneous velocities of the bubbles. The plot indicates that the average velocity of the bubbles continue to increase even after the bubbles lift-off from the wall. It also reveals that the time it takes for the bubbles to coalesce increases, as the spacing between the bubble increase.

It is also seen that the bubble pair with initial spacing of 0.1 mm coalesced before departing from the wall while the others experienced lift-off before merging inside the subcooled liquid. A sudden rise and drop in velocity is observed immediately after the bubbles coalesce as given at approx. 2.2, 3.8, & 9 ms for the bubbles with initial spacing of 0.1, 0.2, & 0.3 mm respectively. The sudden velocity drop in Fig. 5(a) occurs due to the sudden bubble size increase resulting in a change in topology and oscillation. Therefore, the bubble tends to decelerate as it undergoes topology change into a more stable shape. The coalescence time was defined as the instant when the bubbles come in contact with each other.

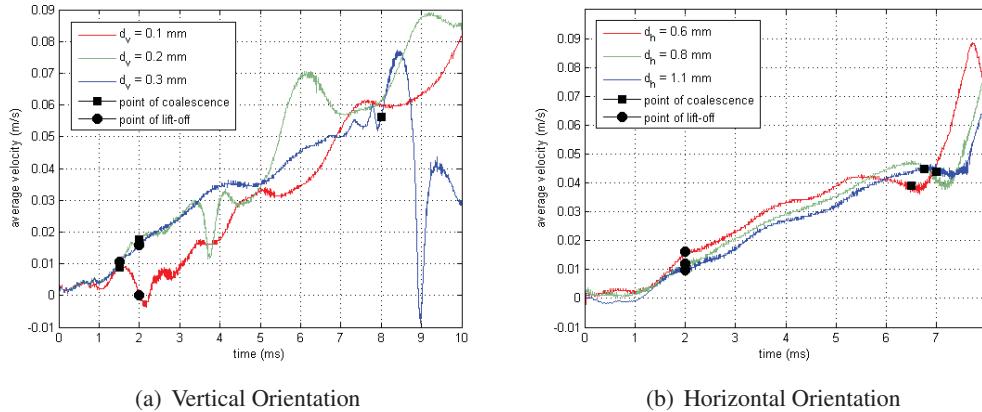


Figure 5: Plots showing effect of spacing and orientation between two consecutive and adjacent bubbles during coalescence

When the bubble are at the same vertical level, the coalescence behavior of the bubbles was also investigated by varying the horizontal spacing between them. As presented in Fig. 5(b), the average velocity of the bubble pairs slightly increases as the spacing between them is reduced. All the bubbles lift-off from the wall at approx. 2 ms, and tend to move towards the center of the cylindrical domain where they coalesce. Sudden velocity rise and drop, and subsequent oscillation is observed after the bubbles coalesce at times of 6.5 – 7 ms, in the order of their initial spacing. The 3-D images of the coalescing bubble pair with the temperature distribution is shown in Fig. 6. They show the changes in topology that newly formed bubbles undergo after coalescing.

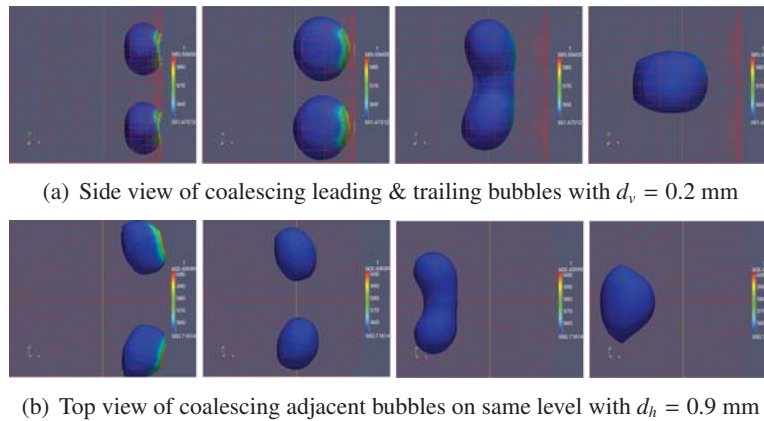


Figure 6: Comparison of bubble coalescence for consecutive bubbles and adjacent bubble pairs

5.2 Effect of System Pressure

Bubble coalescence behavior was then studied when the system pressure was varied. Fig. 7(a) reveals the average bubble velocity between 1 – 21 MPa at zero bulk velocity. It shows that the average velocity increases as system pressure was raised. The plot also reveals that all the bubble pairs lifted off from the wall before coalescing with lift-off time increasing as system pressure increased.

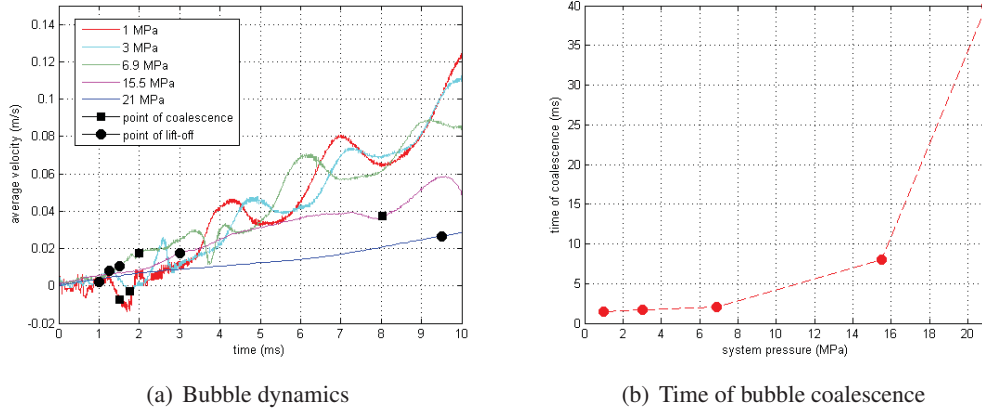


Figure 7: Plots showing effects of system pressure on bubble dynamics and time of coalescence

It is also observed that the time for the bubbles to coalesce increases rapidly with system pressure, as shown in Fig. 7(b). The bubble at 21 MPa did not coalesce even after 40 ms. This trend occurs due to the low liquid-vapor density ratio at higher pressure forcing the bubbles to grow at a slower rate. This makes the leading bubble have smaller wakes thereby resulting in slower distance reduction between the bubble pair and longer time for them to coalesce.

5.3 Effect of Bubble Size

Next, the sizes of the bubbles were varied between 0.25 – 0.75 mm diameter with the same initial spacing. Velocity plot of the bubbles before and after coalescence is given in Fig. 8. The 0.25 mm diameter bubble pair departed from the wall the fastest but also took the longest time to coalesce. It then experienced a sharp drop in velocity due to the topology change and oscillation after coalescence.

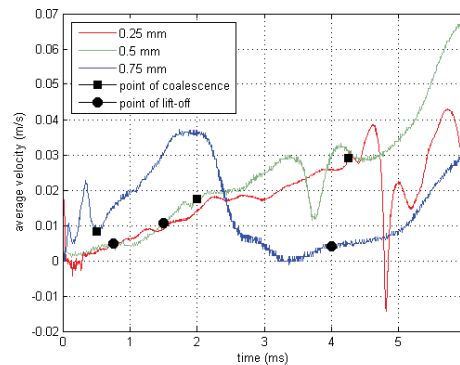


Figure 8: Effect of bubble size on bubble coalescence

The 0.75 mm diameter bubble pair coalesced at the wall due to their large size relative to the initial spacing as presented in Fig. 9(a). The coalesced bubble experienced multiple changes in topology and oscillations. It only departed from the wall after 4 ms. The topology of the 0.75 mm bubble changed from ellipsoidal and to ellipsoidal cap while the new bubble from the merged 0.25 mm diameter bubbles in Fig. 9(b) maintained an ellipsoidal shape after coalescence.

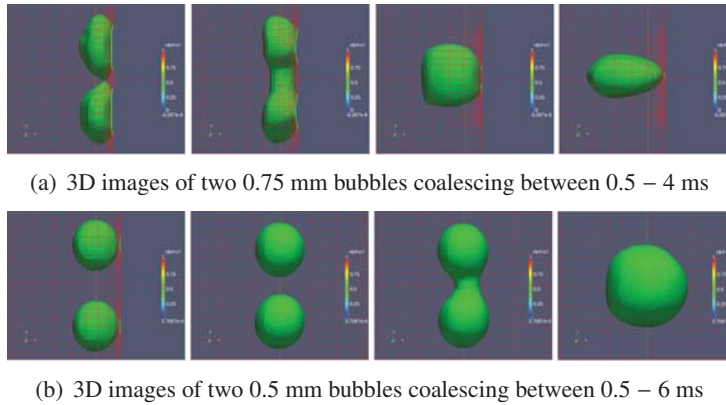


Figure 9: Comparison of bubble coalescence process for two consecutive bubbles of different initial sizes

5.4 Effect of Bulk Velocity

The bubble coalescence behavior was then investigated by varying the velocity of the bulk fluid while maintaining other flow conditions of the base case. The average velocity of the bubbles relative to the bulk velocity was compared as shown in Fig. 10(a). The plot reveals that relative average velocity of the bubbles decreased as the bulk velocity was raised, due to the increased turbulence around the bubble. All the bubbles experienced lift-off before coalescence. The bubble pair at 5 m/s bulk had the fastest time of coalescence while bubble pair at 0.5 m/s has the slowest. However, bubble pairs at bulk velocities of 1 & 2 m/s did not coalesce.

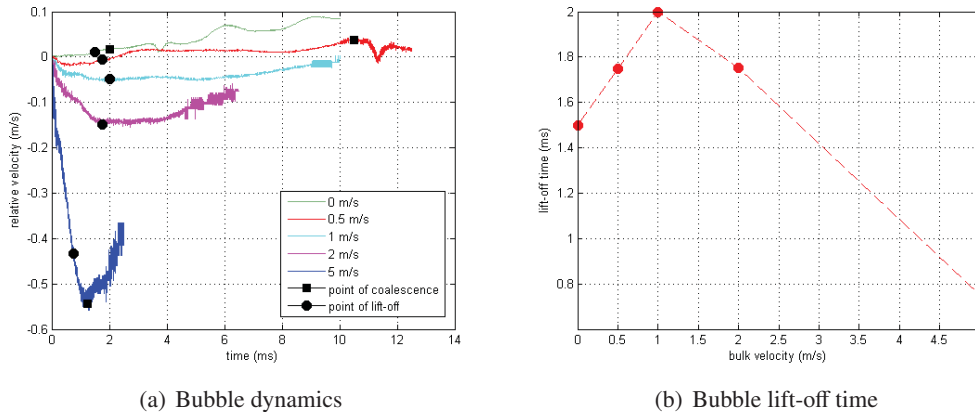


Figure 10: Plots showing effects of bulk velocity on bubble dynamics and lift-off time during coalescence

Variation of the lift-off time with the bulk velocity is given in Fig. 10(b). It shows that lift-off time of the bubbles peaked at 1 m/s bulk and then decreases as the bulk velocity was further increased. This non-linear behavior occurs because bubble growth rate is higher at lower velocity leading to faster lift-off. However, this effect diminishes as the bulk velocity is raised due to the increase in near-wall turbulence around the bubble.

The flow characteristics around the bubble pair as they coalesce, at bulk velocities of 0 & 5 m/s is given in Fig. 11 & 12, respectively. The images in Fig. 11 show the flow characteristics for the stages of bubble coalescence at time interval of 1.5 & 3 ms, using a bulk velocity of zero. It reveals an increase in

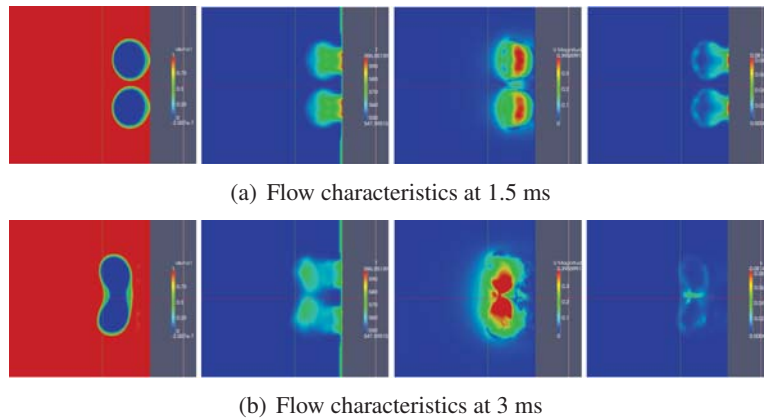


Figure 11: Comparison of void fraction, temperature, velocity, & turbulent kinetic energy fields, between two coalescing bubbles at zero bulk

velocity at the thin liquid film between the bubbles as they coalesce. Fig. 12 also compares the flow behavior at a the point of coalescence at time interval of 1 & 1.5 ms, using a bulk velocity of 5 m/s. The bubble shape after merging is as a result of the strong flow stream and turbulence near the wall. Compared to the case at zero bulk, the images show a faster convection of temperature from the wall, thereby reducing the bubble growth rate.

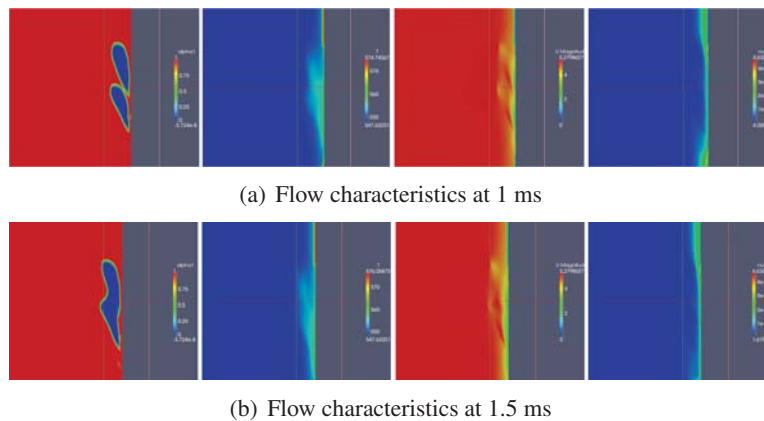


Figure 12: Comparison of void fraction, temperature, velocity, & SGS kinematic viscosity fields, between two coalescing bubbles at 5 m/s bulk velocity

6. CONCLUSIONS

The coalescence of two bubbles in subcooled flow boiling was numerically studied using water and steam as the working fluid. The results indicate that the bubble coalescence time increases at higher system pressure. The lift-off time of the bubbles from the wall initially increased as bulk velocity was raised and peaked at 1 m/s. However, the lift-off time decreased upon further bulk velocity increase. The average velocity decreased at higher bulk velocity and system pressure. It was also observed that a newly formed bubble experiences sudden rise and drop in velocity after coalescence, due to the volume increase. This results in topology change and oscillation of the bubble until it attains a stable shape.

References

1. J. Wei, L. Pan, D. Chen, H. Zhang, J. Xu, and Y. Hu, Numerical simulation of bubble behaviors in subcooled flow boiling under swing motion. *Nucl. Eng. Des.* **Vol. 241**, pp. 2898–2908 (2011).
2. G. H. Yeoh and J. Y. Tu, A unified model considering force balances for departing vapour bubbles and population balance in subcooled boiling flow. *Nucl. Eng. Des.* **Vol. 235**, pp. 1251 – 1265 (2005).
3. J. Bonjour, M. Clause, and M. Lallemand, Experimental study of the coalescence phenomenon during nucleate pool boiling. *Exp. Thermal Fluid Sci.* **Vol. 20**, pp. 180–187 (2000).
4. R. Situ, Y. Mi, M. Ishii, and M. Mori, Photographic study of bubble behaviors in forced convection subcooled boiling. *Int. J. Heat Mass Transfer*. **Vol. 47**, pp. 3659–3667 (2004).
5. I. Golobic, J. Petkovsek, and D. B. R. Kenning, Bubble growth and horizontal coalescence in saturated pool boiling on a titanium foil, investigated by high-speed ir thermography. *Int. J. Heat Mass Transfer*. **Vol. 55**, pp. 1385 – 1402 (2012).
6. R. H. Chen, W. X. Tian, G. H. Su, S. Z. Qui, Y. Ishiwatari, and Y. Oka, Numerical investigation on coalescence of bubble pairs rising in a stagnant liquid. *Chem. Eng. Sci.* **Vol. 66**, pp. 5055 – 5063 (2011).
7. H. G. Weller, G. Tabor, H. Jasak, and C. Fureby, A tensorial approach to computational continuum mechanics using object-oriented techniques. *Computers Phys.* **Vol. 12**, pp. 620–631 (1998).
8. E. Berberovic, N. P. van Hinsberg, S. Jakirlic, I. V. Roisman, and C. Tropea, Drop impact onto a liquid layer of finite thickness: Dynamics of cavity evolution. *Phys. Rev. E*. **Vol. 79**, p. 036306(15) (2009).
9. B. Weigand, J. R. Ferguson, and M. E. Crawford, An extended Kays and Crawford turbulent Prandtl number model. *Int. J. Heat Mass Transfer*. **Vol. 40**, pp. 4191–4196 (1997).
10. J. Wu and V. J. Dhir, Numerical Simulation of the Dynamics and Heat Transfer Associated With a Single Bubble in Subcooled Pool Boiling. *J. Heat Transfer*. **Vol. 132**, pp. 111501–15 (2010).
11. C. Fureby, G. Tabor, H. G. Weller, and A. D. Gosman, A comparative study of subgrid scale models in homogeneous isotropic turbulence. *Phys. Fluids*. **Vol. 9**, pp. 1416–1429 (1997).
12. D. B. Spalding, A single formula for the "law of the wall". *J. Applied Mechanics*. **Vol. 28**, p. 455 (1961).
13. N. E. Todreas and M. S. Kazimi, *Nuclear Systems I: Thermal Hydraulic Fundamentals*. Taylor & Francis Group, New York (1990).
14. P. C. Duineveld, Bouncing and coalescence of bubble pairs rising at high reynolds number in pure water or aqueous surfactant solutions. *Appl. Sci. Res.* **Vol. 58**, pp. 409 – 439 (1998).
15. M. Kemiha, N. Dietrich, S. Poncin, and H. Z. Li, Coalescence between bubbles in non-newtonian media. Montreal, Canada (2009).
16. R. V. Chaudhari and H. Hofmann, Coalescence of gas bubbles in liquids. *Rev. Chem. Eng.* **Vol. 10**, pp. 131–190 (1994).